Showcasing research from Professor Günther Rupprechter's laboratory, Institute of Materials Chemistry, Technische Universität Wien, Vienna, Austria.

Sum frequency generation spectroscopy in heterogeneous model catalysis: a minireview of CO-related processes

Xia Lia and Günther Rupprechter report how polarization-dependent sum frequency generation (PD-SFG) vibrational spectroscopy is applied to ambient pressure surface science studies of adsorbates and catalytic reactions at solid/gas interfaces. Combined with SFG modeling, low energy electron diffraction (LEED) and density functional theory (DFT) calculations, chemical species and their molecular structures, coverages and orientations at the surface of single crystal and nanoparticle model catalysts can be identified.

ROYAL SOCIETY
OF **CHEMISTRY**

rsc.li/catalysis

MINI REVIEW

Check for updates

Sum frequency generation spectroscopy in heterogeneous model catalysis: a minireview of CO-related processes

Xia Li [iD] and Günther Rupprechter [iD]*

Sum frequency generation (SFG) vibrational spectroscopy is a unique surface/interface-sensitive method, enabling the identification of chemical species and molecular structures, densities and orientations. SFG has been proven to be a powerful probe to examine adsorbates and reactions at solid–gas interfaces related to heterogeneous catalysis, employing well-defined ultra-high vacuum (UHV) grown model catalysts and UHV-compatible high-pressure reaction cells, enabling bridging both the materials and pressure gaps. SFG was thus among the first methods for ambient pressure surface science, enabling the characterization of "high pressure adsorbates". In this mini-review, we provide an overview of SFG studies

Institute of Materials Chemistry, Technische Universität Wien, 1060 Vienna, Austria. E-mail: guenther.rupprechter@tuwien.ac.at; Tel: +43 (1) 58801 165100

Xia Li received her Master's degree in Polymer Chemistry and Physics at Qingdao University of Science and Technology (Shandong, China) and obtained her Ph.D. in Physical Chemistry from the Institute of Chemistry, Chinese Academy of Sciences (Beijing, China). In 2016, she started a postdoctoral position at the Technische Universität Wien (Vienna, Austria) in the group of Günther Rupprechter. In her current research she uses polarization-dependent sum frequency generation (SFG) vibrational spectroscopy, low energy electron diffraction (LEED) and Auger electron spectroscopy (AES) to reveal adsorbate/reactant structures and orientations on model catalyst surfaces (e.g. Pt, Pd, and Ir single crystals and graphene-supported nanoparticles). Since 2019, she holds a Lise Meitner Fellowship of the Austrian Science Fund (FWF).

Xia Li

Günther Rupprechter received his Ph.D. in Physical Chemistry from the University of Innsbruck (Austria). After being a postdoctoral fellow at the University of California at Berkeley and the Lawrence Berkeley National Laboratory (with Gabor A. Somorjai), he became group leader for Laser Spectroscopy and Catalysis at the Fritz Haber Institute of the Max Planck Society in Berlin (Germany) from 1999 to 2005 (with Hajo Freund). In 2005, he accepted a full professorship in Surface and Interface Chemistry at Technische Universität Wien (Austria). His research emphasis is on heterogeneous catalysis, particularly in situ (operando) spectroscopy/microscopy on model and technological catalysts, applied to studies of the mechanisms and kinetics of processes relevant for energy and the environment: hydrogen as clean fuel, methane reforming, CO_2 hydrogenation and more efficient automotive pollution abatement. In 2005, he received the Jochen Block Award of the German Catalysis Society for "the application of surface science methods to heterogeneous catalysis" and became a corresponding member of the Austrian Academy of Sciences in 2012. He is an editorial board member of "Catalysis Letters" and "Topics in Catalysis", and Vice-Chair of the Austrian Catalysis Society. Since 2018 he is a "Renowned Overseas Professor" of Shanghai University of Engineering Science.

Günther Rupprechter

12 | *Catal. Sci. Technol.*, 2021, **11**, 12–26

This journal is © The Royal Society of Chemistry 2021

of CO-related processes in heterogeneous model catalysis. This includes pressure- and/or temperature-dependent CO adsorption on single crystals (platinum, palladium, rhodium, iridium, copper, nickel) and oxide/graphene-supported (palladium, platinum) nanoparticles, as well as CO reactions (oxidation/hydrogenation) simultaneously monitored by SFG and mass spectrometry. The adsorption of isotopic CO mixtures on single crystals and nanoparticles provides information on the individual contributions of vibrational coupling and chemical interactions to the adsorbate–adsorbate interactions. Altogether, SFG helps to identify various adsorption sites, adsorbate structures, molecular orientations and CO reactions on prototypical catalyst surfaces of increasing complexity. Specifically, the analysis of molecular orientation (tilt angles) can be carried out by polarization-dependent SFG.

1. Introduction: SFG in heterogeneous catalysis

Surface science has to a large extent been driven by heterogeneous catalysis,[1–8] which mostly occurs at solid–gas interfaces (for solid–liquid interfaces we refer to ref. 9–12 and references therein). Much of the fundamental understanding of elementary steps originates from studies of well-defined model catalysts in ultrahigh vacuum (UHV),[1,2] especially when combined with DFT calculations.[13–20] Investigations of metal single crystal surfaces of different crystallographic orientations directly revealed the structure-sensitivity of gas adsorption, co-adsorption and reactivity, focusing on molecular/dissociative adsorption and oxidation/hydrogenation reactions.

This was based on an arsenal of tools, but most of the typical surface-sensitive methods require UHV, such as low energy electron diffraction (LEED), Auger electron spectroscopy (AES), temperature programmed desorption/reaction (TPD/R), X-ray/UV photoelectron spectroscopy (XPS/UPS), electron energy loss spectroscopy (EELS), infrared reflection absorption spectroscopy (IRAS), and others.

UHV conditions guarantee the cleanliness of the surfaces and well-controlled conditions, but due to the low-pressure cryogenic temperature (liquid N_2) needed to produce substantial surface coverages of adsorbates, at such low temperatures, adsorbate structures may be different[21] and reactions typically do not occur. *Vice versa*, at high temperatures of catalytic reactions, coverages under UHV are typically very low, whereas technological catalytic reactions are carried out at ~10 orders of magnitude higher pressure. Accordingly, it was debated whether the adsorbed species observed under UHV conditions are really comparable to the "high pressure species" present under reaction conditions. The pressure differences may also affect the chemical state of a catalyst surface under reaction conditions (*e.g.* by oxidation, hydride formation, coking, restructuring, *etc.*). Both effects lead to the so-called pressure gap.

Over the years, several surface-sensitive and UHV-compatible methods have been developed that are able to operate under (near) atmospheric pressure, *e.g.* sum frequency generation (SFG) laser spectroscopy, polarization-modulation infrared reflection absorption spectroscopy (PM-IRAS), near ambient pressure X-ray photoelectron spectroscopy (NAP-XPS), high-pressure scanning tunnelling microscopy (HP-STM) or surface X-ray diffraction (SXRD). To examine UHV-grown model catalysts at realistic pressure and temperature *via* ambient pressure surface science, dedicated UHV-compatible high-pressure cells have thus been constructed.[22–30]

Together with advances in model catalyst preparation, the pressure (UHV *vs.* atmospheric pressure), material (single crystals *vs.* supported nanoparticles), and complexity (alloys, promoters, multicomponent oxides) gaps between surface science and applied catalysis have been substantially narrowed, but understanding catalysis at the atomic level remains a formidable task.

Along these lines, sum frequency generation (SFG) spectroscopy, exhibiting utmost surface sensitivity[31] as the SFG process solely occurs at a surface or interface, has been performed using UHV-compatible high-pressure cells. SFG has been successfully employed to understand molecular level gas adsorption/reaction (*e.g.* adsorption sites, adsorbate structures, orientations, and changes thereof) on model catalyst surfaces.[6,32–34] The initial surface science SFG studies examined the adsorption of small molecules (such as CO, NO or alkenes) on metal single-crystal surfaces (such as Pd(111),[35] Pd(100),[36] Pt(111),[37–39] and Rh(111)[40]). The SFG vibrational spectra provided insight into adsorption sites and adsorption configurations up to atmospheric pressure, for example the relative population of hollow/bride/on-top bonded CO or di-σ/π bonded ethylene/propylene.[41–44] Subsequently, SFG has also been employed to study the structure of adsorbates on polycrystalline foils,[45,46] thin films,[47] and supported nanoparticles (NPs of Pd, Pt, *etc.*),[6,35] extending typical UHV surface science experiments to more realistic pressures and temperatures.

The "drosophila" molecule CO has been frequently used as a probe to "titrate" the number and nature of exposed metal atom/sites of a catalyst, but CO is also involved in many processes of environmental and energy catalysis (exhaust cleaning, reforming, water gas shift, Boudouard, methanation, methanol synthesis, Fischer–Tropsch, *etc.*). In the following, we will thus focus on rather recent SFG studies of CO adsorption and reaction on metal single crystals and supported nanoparticles. Note that there are also reports of applying SFG to technological catalysts (powders) and shape-controlled colloidal nanoparticles linked to quartz prisms,[48–53] with total internal reflection geometry yielding a higher signal.

Before turning to the details of SFG, we would like to stress that there are a number of other, often

This journal is © The Royal Society of Chemistry 2021

Catal. Sci. Technol., 2021, **11**, 12–26 | **13**

complementary, methods that can operate under near ambient pressures (NAP). They include *e.g.* vibrational spectroscopy (polarization modulation (PM) IRAS), composition (X-ray photoelectron spectroscopy; NAP-XPS[54,55]) and structure characterization (surface X-ray diffraction (SXRD),[56,57] electron microscopy[58] and scanning tunnelling microscopy[55,59]). These methods, which can be applied to both solid/gas and solid/liquid interfaces, were previously contrasted to SFG.[6] For more detailed accounts we refer to a number of recent reviews.[60–63]

2. SFG theory

SFG is a second order nonlinear optical process and in a "conventional scanning" setup, a tunable infrared beam is mixed with a (fixed-frequency) visible beam to generate a sum frequency output (Fig. 1). The SFG output is thus in the near-infrared or visible region and can be detected by a photomultiplier.[31] In the electric dipole approximation, the mixing process is allowed only in a medium without centrosymmetry, thus it is restricted to the surface (or interface), where the symmetry is broken (surface-specificity). When the IR beam (ω_{IR}) is tuned through a vibrational resonance of the adsorbate, it induces a vibrational transition from the ground state ($v = 0$) to an excited state (*e.g.* $v = 1$), and simultaneously the visible beam (*e.g.* $\omega_{Vis} = 532$ nm) induces a transition to a higher-energy virtual state through an anti-Stokes Raman process (Fig. 1 inset). When the virtual state relaxes, light is generated at the sum of the two incident frequencies ($\omega_{SFG} = \omega_{Vis} + \omega_{IR}$) (Fig. 1). To acquire an SFG vibrational spectrum of adsorbate molecules (*e.g.* CO) on a metal catalyst (*e.g.* Ir(111) single crystal), the IR and visible beams are spatially and temporally overlapped on the sample. The beam mixing process induces a nonlinear polarization ($P^{(2)}$):[64]
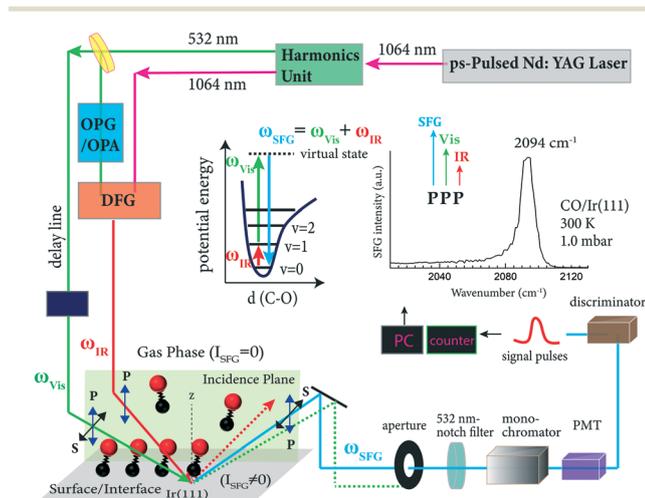

Fig. 1 Schematic illustration of the IR-vis SFG measurement, using CO adsorption on Ir(111) as an example. The energy level diagram of an IR single-resonance SFG process and an exemplary SFG spectrum of CO/Ir(111) are shown as insets (right inset adapted from Li *et al.*[32] with permission. Copyright (2020) American Chemical Society).

$$P^{(2)}(\omega_{SFG}) = \chi_S^{(2)} E(\omega_{Vis}) E(\omega_{IR}), \qquad (1)$$

with $\chi_S^{(2)}$ being the surface nonlinear susceptibility and $E(\omega_{Vis})$ and $E(\omega_{IR})$ being the magnitudes of the local electric fields. The intensity of the SFG signal (I_{SFG}) generated by the nonlinear polarization is proportional to the absolute square of $\chi_S^{(2)}$ and to the product of the incident light intensities:

$$I_{SFG} = |\chi_S^{(2)}|^2 I_{Vis} I_{IR}. \qquad (2)$$

The term $\chi_S^{(2)}$ is composed of two components: a nonresonant nonlinear susceptibility $\chi_{NR}^{(2)}$ from the surface itself (*e.g.* electronic transitions in Ir(111)) and a resonant nonlinear susceptibility $\chi_R^{(2)}$ from the adsorbate (CO) vibrations. In many cases, the applied input frequencies are far from resonances of the surface, and the response of the surface is therefore usually modeled by a frequency-independent nonresonant susceptibility (assuming that this also incorporates the nonresonant contribution from higher-order multipole moments of the centrosymmetric bulk). Consequently,

$$\chi_S^{(2)} = \chi_{NR}^{(2)} + \chi_R^{(2)} = A_{NR} e^{i\phi} + \sum_q \frac{A_q}{\omega_{IR} - \omega_q + i\Gamma_q}, \qquad (3)$$

where A_{NR} is the amplitude of the $\chi_{NR}^{(2)}$, and ϕ is its phase relative to the resonant term. A_q, ω_q, and Γ_q are the amplitude, resonance frequency, and damping constant (homogeneous linewidth $2\Gamma_q$ = full width at half maximum (FWHM)) of the qth vibrationally resonant mode $\chi_R^{(2)}$. The term $\chi_R^{(2)}$ incorporates the resonance condition ($\omega_{IR} - \omega_q$), and as ω_{IR} is close to ω_q, $\chi_S^{(2)}$ should exhibit a resonant enhancement. Thus, by continuous tuning of the IR beam and monitoring the intensity of the SFG output, an adsorbate vibrational spectrum is obtained as a plot of the SFG intensity against the IR wavenumber (Fig. 1 inset).

The polarizations of both incidence and output beams can be switched between P- and S-polarization. P denotes the polarization of the optical field in the incidence plane, and S denotes the polarization of the optical field perpendicular to the incidence plane (Fig. 1). Because $\chi_S^{(2)}$ is polarization-dependent, SFG measured in different polarization combinations (*e.g.* SSP, PPP, SPS, PSS) yields different information (see below). PPP denotes the polarization combinations in the order of relative laser energies: that is, SFG, visible and IR beams (Fig. 1 inset). For metal surfaces, the IR laser beam must always be P-polarized, because the surface electric-field of an S-polarized IR laser beam is screened by the conduction electrons of the metal. In contrast, the polarization of the visible and SFG beams can be switched between S and P due to the lower dielectric constants of metals in the visible region, which is why the surface electric field is less effectively screened by the conduction electrons.[65]

Because $\chi_{NR}^{(2)}$ contributes to $\chi_S^{(2)}$, an observed spectrum may appear somewhat "distorted" (asymmetric, negative/derivative) peaks, resembling coherent anti-Stokes Raman spectra, but being quite different from IR spectroscopy.

14 | *Catal. Sci. Technol.*, 2021, **11**, 12–26

This journal is © The Royal Society of Chemistry 2021

Depending on the (relative) amplitudes (A_{NR} and A_q), and the phase shift, the SFG lineshape may be strongly asymmetric.[66] In particular for metal or semiconductor interfaces, incorporation of inhomogeneous effects on the lineshape must be considered. However, the simple assumption of a Lorentzian line profile in eqn (3) can be successfully applied in spectral fitting.

The amplitude of the vibrationally resonant susceptibility A_q is related to the adsorbate concentration (surface density of molecules, N_s) and the microscopic hyperpolarizability tensor elements $\beta_q^{(2)}$ in the molecular coordinates system:

$$A_q = N_s \langle \theta, \psi, \phi \rangle \beta_q^{(2)} \tag{4}$$

$\langle \theta, \Psi, \phi \rangle$ representing an ensemble average over all possible molecular orientations:[67] tilt angle (θ), twist angle (Ψ) and azimuthal angle (ϕ). For a vibrational mode to be SFG active, it must simultaneously satisfy both IR and Raman selection rules, because $\beta_q^{(2)}$ is a function of the Raman polarizability tensor and the IR transition dipole moment of the qth vibrational mode.

In general, for $C_{\infty v}$ (e.g. single OH, CH bond, CO molecules) and C_{3v} (e.g. CH_3, NH_3, SiH_3 groups) groups, the twist angle (Ψ) and azimuthal angle (ϕ) can be integrated, and only the tilt angle needs to be determined. However, if a symmetric stretch vibrational mode of a CH_2 group is observed in the SPS and PSS polarizations, the twist angle Ψ cannot be rotationally averaged anymore.[68]

Concerning polarization-dependent measurements, an SFG signal is generated only when the electric fields of the visible and IR lights have a component parallel to the bond axis of the adsorbed molecule.[69] Consequently, PPP spectra detect molecules with molecular axes parallel or inclined to the surface normal, whereas SSP spectra are mainly sensitive to molecules tilted relative to the macroscopic surface normal (e.g. for CO/Ir(111),[32] the SSP intensity is maximum for a tilt angle of 51° with $R = 0.08$). Utilizing the intensity ratio in different polarization combination spectra (e.g. PPP/SSP), or the ratio of $CH_{3\text{-sym}}/CH_{3\text{-asym}}$ of the PPP spectrum, the orientation angle of adsorbates can be quantitatively determined.[32,33,46]

In addition, SFG spectroscopy has also been widely applied for solid–liquid interfaces[9–12,70,71] and liquid–liquid interfaces,[72–78] related to electrochemistry, polymers, surfactants, biomolecules and others, and has been extended to SFG microscopy.[46,79,80]

3. UHV-compatible high-pressure reaction cell for SFG spectroscopy

Surface-specific SFG provides vibrational spectra of surface adsorbed molecules only, while molecules in the gas phase do not produce signals. Consequently, SFG is perfectly suited for spectroscopy from UHV to atmospheric pressure (IR gas phase absorption must still be accounted for; for details see ref. 6). Fig. 2a shows an UHV-compatible high-pressure
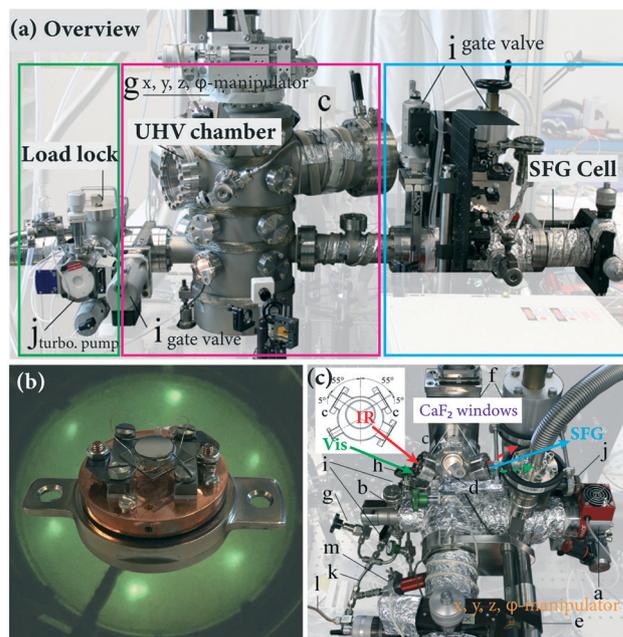

Fig. 2 SFG spectroscopy on model catalysts from UHV to 1 bar: (a) overview of the three main sections, connected via magnetic transfer rods: load-lock, UHV preparation/characterization chamber and UHV-high-pressure spectroscopic SFG cell. (b) Photograph of the sample holder with an Ir(111) single crystal mounted, with the corresponding LEED pattern as background. (c) Photograph of the SFG spectroscopic cell, displaying the beam input/exit CaF$_2$ windows. (a) and (c) are adapted from Roiaz et al.[28] with permission. Copyright (2018) American Institute of Physics.

reaction cell, optimized for SFG spectroscopy, and attached to a UHV preparation/analysis chamber for heterogeneous model catalysts (a thorough description can be found in ref. 28). Briefly, this setup has three main sections:

i) A load-lock to quickly insert samples into the system, without the need to vent the main UHV chamber.

ii) A main UHV chamber to prepare and characterize model catalyst surfaces.

iii) An SFG high-pressure cell (that can be operated from UHV to 1 bar) to measure the vibrational spectra of molecular adsorbates.

The UHV chamber (base pressure $<5 \times 10^{-10}$ mbar) is a stainless-steel vessel of about 40 L volume equipped with various flanges to accommodate analysis and preparation tools (e.g. LEED/AES (c), mass spectroscopy (MS), evaporator, microbalance, etc.) and gauges, with connections and gate valves to/between the load-lock and SFG cell. The sample, such as an Ir(111) single crystal (disk-shaped, 6 mm outer diameter), is mounted onto the sample holder (Fig. 2b), which allows heating by Joule resistive heating to 1273 K and cooling to 95 K (LN$_2$). After installation in the load-lock and transfer to the UHV manipulator using a magnetic transfer rod, the single crystal is pretreated in the UHV chamber by cycles of Ar ion-sputtering, O$_2$ oxidation and annealing.[28,33] The long-range surface ordering and cleanliness of the pretreated Ir surface are confirmed by LEED and AES, respectively. After the cleaning procedure, the sample is

This journal is © The Royal Society of Chemistry 2021

Catal. Sci. Technol., 2021, **11**, 12–26 | **15**

further transferred to the SFG spectroscopic cell for measurements, as shown in Fig. 2c.

The SFG cell, shown in Fig. 2c has a volume of approximately 1.5 L. It is pumped by a combination of a turbomolecular pump (j) and a pre-vacuum diaphragm pump (to prevent oil back-diffusion) to a routine base pressure of 1 × 10^{-9} mbar. The x, y, z, φ-manipulator (e) of the SFG cell, receiving the sample holder, allows optimization of the sample position, ensuring a spatial overlap of the visible and IR impinging beams on the surface. Two CaF$_2$ windows (c) allow directing the visible and IR laser radiation into the cell and the SFG signal to exit to the detector. According to the SFG geometry, the windows are oriented at 55° with respect to the surface normal. Furthermore, the window surface normal is tilted 5° off the incidence laser beams to avoid back-reflection into the laser optics. A third window (d) is placed on-top of the sample stage to visually inspect the position during sample transfer and SFG measurements. A gas (mixture) at 1000 mbar is recirculated in the SFG cell by a metal-bellows pump (i).

Although no SFG signal is produced by the gas phase itself, at elevated pressure significant frequency-dependent IR absorption occurs in the gas phase *via* vibrational and rotational excitations. Consequently, because the number of generated SFG photons depends linearly on the intensity of the IR pulse (and the visible, which, however, is essentially constant), the SFG process is indirectly influenced by the gas pressure.[6] However, the distance between the input window and the sample is only 5.4 cm (Fig. 2c), which is why there is hardly any gas-phase IR-absorption at CO pressures below 200 mbar.

For the SFG laser spectrometer, most frequently neodymium–yttrium–aluminum–garnet (Nd:YAG), titanium–sapphire (Ti:Sa) or free-electron lasers are used. For details on the generation of tunable IR and visible radiation and on the detection of the SFG signal, we refer to ref. 6 and references therein. A 20 ps mode-locked Nd:YAG-based "scanning" system (EKSPLA; 1064 nm, 30 mJ per pulse, 50 Hz repetition rate) is briefly described here and depicted schematically in Fig. 1. The output of a 1064 nm picosecond laser is partly converted to 532 nm light by a second-harmonic generator (SHG). One part of 532 nm is used as the visible input for the surface SFG experiment. Another part of the 532 nm beam is used to pump an optical parametric generator/amplifier (OPG/OPA). The generated tunable near-IR idler and another portion of 1064 nm are spatially and temporally overlapped in a difference frequency generation (DFG) crystal (*e.g.* AgGaS$_2$), generating the tunable mid-IR beam (2.3–10 μm) for the SFG process. The polarization of the visible light and SFG signal is switched between P and S using a Glan–Taylor prism and a half-wave plate, while the infrared polarization is always kept as P (an S-polarized field would be canceled on a metal surface[65]). The used beam energies for CO/single crystals (Ir, Pt, Pd)[32,33] are approximately 40 μJ per pulse for visible and 90–130 μJ per pulse for IR between 1800 and 2160 cm^{-1}. The angle of incidence of a laser beam has a significant effect on the SFG intensity[33] and was usually around 55°. However, a difference in the incident angles is necessary to separate the SFG signal from the reflected pump beams by an aperture (Fig. 1). A 5° angular separation between IR and visible beams is sufficient for spatially filtering the reflected input light from the SFG signal.[64] To better remove contributions from the reflected pump beams, a combination of spatial, spectral and temporal filtering is required.[6,81] Therefore, the SFG signal is filtered by an aperture, notch filter, monochromator, detected by a photomultiplier tube (PMT) and (gated) discriminator, and finally recorded using software (Fig. 1).

4. Case studies

4.1 CO adsorption on single crystals

4.1.1 Pressure- and temperature-dependent SFG spectra: CO adsorption sites. For a long time, studies of molecules adsorbed on single crystals were restricted to IRAS and EELS, which had to be operated under UHV. Adsorbate structures on model catalysts under technologically-relevant atmospheric pressure were thus unknown. Nearly 25 years ago, Su *et al.*[38] reported SFG studies of CO adsorption on Pt(111) at 295 K. At low pressures (<10^{-7} Torr) CO binds on-top of Pt atoms (2095 cm^{-1}) and at bridge sites (1845 cm^{-1}), with on-top CO dominating the PPP spectra, since the bridge CO signal is several times weaker than the on-top CO signal. Similar observations were reported at 150 K by Daum and coworkers[82] and at 300 K by Williams *et al.*[39] As pressure increased, the frequency of on-top species shifted to a high value (2105 cm^{-1}, Fig. 3a) due to enhancement of dipole coupling between CO molecules on the surface.[38] At 4 and 400 mbar CO at room temperature (Fig. 3a), on-top CO at terrace sites still dominates the SFG spectra, in accordance with the study of CO in the pressure range 10^{-7} to 100 mbar at 300 K by Carrasco *et al.*[83] Additionally, there is a small shoulder at 2073 cm^{-1} at 4 mbar attributed to on-top CO at step sites,[33] as the frequency of on-top CO is lower for lower coordination numbers of surface atoms, *e.g.* 2065 cm^{-1} for low coverage on Pt(110), whereas it is 2083 cm^{-1} on Pt(111).[82] Overall, the species observed were the same as those under UHV (*i.e.* there were no new "high pressure species"), but the coverage and ordering sensitively depended on pressure. For example, at 250 K two on-top signals at 2109 cm^{-1} and 2093 cm^{-1} were reported, originating from different CO compression layers on Pt(111) at coverages >0.5 ML.[83]

When Rh(111) was exposed to a high CO pressure up to 1000 mbar (Fig. 3b), additional "lower-frequency" on-top CO stretching vibrational features were observed in SFG,[84] which were absent under UHV conditions, likely due to hollow site population and surface roughening.[37] Spectra acquired after CO pressure evacuation to 10^{-6} mbar were irreversible, however, likely due to CO dissociation.

For CO on Pd(111) under UHV (1 × 10^{-7} mbar), three peaks at 1890, 1925, and 2106 cm^{-1}, characteristic of the stretch vibrations of CO adsorbed at hollow, bridge, and atop
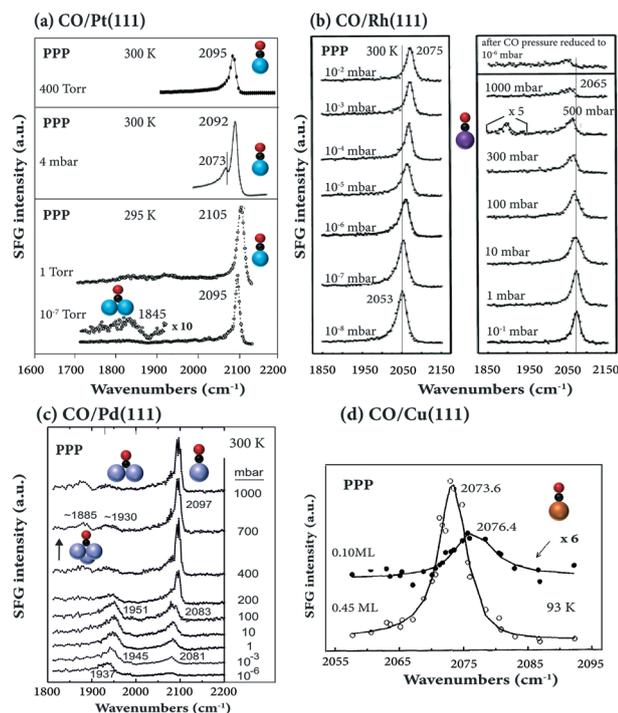
16 | *Catal. Sci. Technol.*, 2021, **11**, 12–26

This journal is © The Royal Society of Chemistry 2021

Fig. 3 Pressure-dependent SFG spectra in PPP polarization combination: (a) CO/Pt(111). 10^{-7} and 1 Torr at 295 K, adapted from Su et al.[38] with permission. Copyright (1996) American Physical Society; 4 mbar at 300 K, adapted from Li et al.[33] with permission from Springer; 400 Torr at 300 K, adapted from Kung et al.[88] with permission from Elsevier. (b) CO/Rh(111) at 300 K, adapted from Pery et al.[84] with permission from Elsevier. (c) CO/Pd(111) at 300 K, adapted from Unterhalt et al.[89] with permission. Copyright (2002) American Chemical Society. (d) CO/Cu(111) at 93 K, adapted from Owrutsky et al.[86] with permission. Copyright (1992) American Institute of Physics.

Fig. 4 Temperature-dependent SFG spectra in PPP polarization combination: (a) CO/Pt(111) in the pressure range of 1×10^{-8}–3×10^{-5} Torr (adapted from Westerberg et al.[91] with permission from Elsevier) and at 4 mbar. (b) CO/Pd(111), after saturating the surface at 90 K, the crystal was annealed as indicated. Adapted from Morkel et al.[21] with permission from Elsevier. (c) CO/Rh(111) at 1 mbar, adapted from Pery et al.[84] with permission from Elsevier. (d) CO/Ir(111) at 1.3×10^{-2} mbar, adapted from Li et al.[32] with permission. Copyright (2020) American Chemical Society.

sites, were observed at 100 K (~0.7 ML coverage).[28] Different from CO on Pt(111)[38] and Rh(111) (Fig. 3b),[37,84] on Pd(111) at room temperature and 6 mbar, the SFG signal of bridge-bound CO is much stronger than that of on-top CO.[28] However, when the pressure exceeds 200 mbar, on-top CO dominates the spectra (Fig. 3c; for details see ref. 6).

For CO on Ir(111),[32,85] Cu(111)[86] (Fig. 3d), Ni(111)[47] and single Fe atoms in a self-assembled 2D metal–organic crystal (Fe-phthalocyanines supported on graphene/Ir(111)[87]), only terminally bound (atop/on-top) CO appeared in the spectra, and other species were not observed.

The temperature-dependence of adsorbed CO on different single crystals is shown in Fig. 4. As temperature increased, the SFG intensity of on-top CO on Pt(111) decreased (in the pressure range of 10^{-8}–10^{-5} Torr). At approximately 460 K, the signal at 10^{-8} Torr was close to zero (Fig. 4a). Previous temperature-programmed desorption (TPD) studies showed that for low exposure (0.5 Langmuir) the desorption maximum is found at 435 K, but shifts to 410 K at a saturation coverage of 4 Langmuir.[90] Accordingly, at higher pressure (4 mbar), the signal of on-top CO disappears at 423 K. When Pt(111) was heated in 400 Torr CO, the vibrational frequency of on-top CO moved to lower wavenumbers and
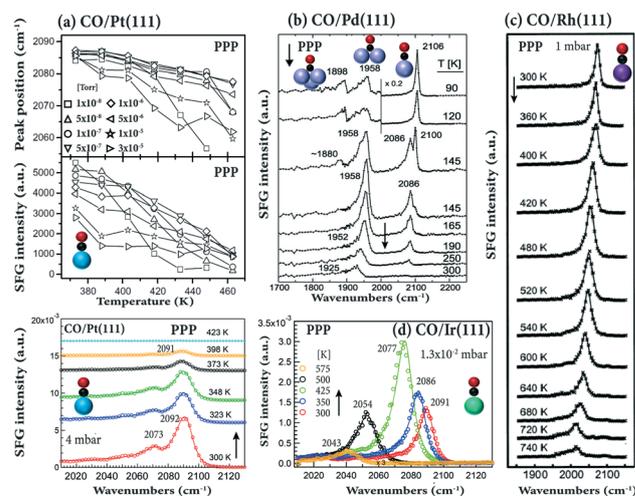
the on-top CO signal disappeared at 823 K.[88] After cooling to room temperature, a strong decrease in spectral intensity was observed, that is, the spectra were irreversible. This was attributed to carbon formation resulting from high-pressure CO dissociation on the Pt(111) surface at 673 K.[88]

Upon heating CO on Pd(111) under UHV (Fig. 4b), the on-top and hollow signals decreased, while that of bridge bonded CO first increased and then decreased. The observed changes can be explained by the complex coverage-dependent adsorption structures of CO/Pd(111), changing from hollow/on-top via bridge/on-top to bridge (for details see ref. 6). This behavior agrees with TPD results indicating that linear CO desorbed at ~275 K (coverage <0.6 ML), whereas the stronger bonded bridge/three-fold hollow CO desorbed at higher temperature (>380 K).[21] SFG spectra of CO on Rh(111) (Fig. 4c) indicated that an additional (but quite weak) low-frequency vibrational feature appeared at temperatures ≥600 K, marking the onset of irreversible CO dissociation.[84]

Distinctively different, upon heating CO on Ir(111), the on-top CO peak in PPP spectra first unexpectedly increased and then decreased (Fig. 4d). The TPD spectra of 0.56 ML coverage CO/Ir(111) in ref. 92 and 93 showed a broad desorption peak, starting at 375 K and extending to 540–600 K, with the peak maximum at 490 K. Therefore, the increase in PPP intensity from 300 to 425 K (despite coverage decreased) suggests a change in the CO tilt angle (see below), while the sharp decrease at 500 K results from CO desorption.[32]

By correlating the SFG intensity with the CO coverage determined from the integrated CO-TPD signal, for CO/Pt foil

a linear relationship of SFG intensity and CO coverage was obtained.[94] However, for on-top (or bridge[95]) CO adsorption on Ni(111),[95] Pt(111)[91,96,97] and Ir(111),[32] non-linear relationships between SFG intensity and coverage were reported. In addition, for CO on Pt(111) and Pt(110),[82] and Ir(111),[32] a decrease in the peak width was observed with increasing CO coverage, due to the formation of uniform overlayer structures at high coverage.[95] Narrow bands at high coverage are indicative of well-ordered uniform overlayer structures.[95]

Because the spectra of CO/Pt(111)[38] and CO/Pd(111)[89] were fully reversible upon variation of the gas pressure, irreversible pressure-induced surface reconstructions were absent (unless Pt(111) was heated at high CO pressure (400 Torr) and high temperature (673 K)[88]). As coverage increased, either by increasing gas pressure or decreasing temperature, the vibrational frequencies of the on-top CO consistently shifted to higher wavenumbers for CO/Pt(111) (Fig. 4a), CO/Pd(111) (Fig. 4b), CO/Rh(111) (Fig. 3b and 4c), and CO/Ir(111) (Fig. 4d). This originates from higher coverage which enhances the dipole–dipole coupling between adsorbed CO molecules and weakens the CO–substrate interaction via donation/back donation (chemical shift). Both effects decrease the strength of the metal–carbon bond, consequently making the C–O bond stronger, shifting the CO resonance position to higher wavenumbers.[32,65,92] For CO/Cu(111) a small opposite shift was observed (2076.4 cm^{-1} at 0.1 ML to 2073.6 at 0.45 ML) (Fig. 3d). Moreover, the phase was constant at 37° for CO/Ir(111),[98] whereas it increases from 20° (0.1 ML) to 30° (0.45 ML) for CO/Cu(111).[86] Note that all SFG spectra discussed so far were measured in PPP polarization combination only.

4.1.2 Orientation of CO on single crystals. For CO molecules adsorbed on metal surfaces, SFG spectra are usually acquired in PPP polarization combination, which typically yields the strongest signal. Using the SSP polarization combination in addition allows the molecular orientation of the adsorbed molecules to be obtained (due to the selection rules the PSP and SPP polarization combinations (relevant for chiral molecules) do not yield a signal on metals[45,99]). However, the SSP signal is normally quite weak, especially when the incidence angles of visible and IR laser beams are not optimized.[33]

For CO on Pt(111),[69] Pd(111)[99] and Ni(111),[47] an upright (perpendicular) orientation of on-top and bridged CO were reported, as in SSP spectra no peaks were observed. Based on the simulations reported in ref. 32 and 33, I_{SSP} is small at $\theta = 0°$, but not zero, at the experimental configurations of $\alpha_{Vis} = 58.5°$ and $\alpha_{IR} = 55°$. Both SSP and PPP spectra of CO/Pt(111) at 300 K were thus obtained with relatively good signal-to-noise ratio (the experimental I_{PPP}/I_{SSP} intensity ratio for on-top CO at terrace sites (2092 cm^{-1}) was 27).[33] The simulated I_{PPP}/I_{SSP} has a maximum at $\theta = 0°$, changing from 20 to 60 for the R-value (i.e. molecular hyperpolarizability ratio) range 0.6–0.3 at $\alpha_{Vis} = 58.5°$ and $\alpha_{IR} = 55°$.[33] Also, the simulated I_{PPP}, I_{SSP}, and I_{PPP}/I_{SSP} significantly depend on the incidence

angles of visible and IR beams (α_{Vis} and α_{IR}). In particular, I_{PPP}/I_{SSP} increased as α_{Vis} increased. Therefore, the absence of SSP signals in previous studies may be due to the use of unfavorable incidence angles of visible and/or IR laser beams.

Taking advantage of the high-pressure capability of SFG, the pressure-dependent PPP and/or SSP spectra for CO on Pt(111) and Pd(111) at 300 K were obtained. PPP and SSP spectra of CO on Pt(111) simultaneously increased with CO pressure (10^{-4}–36 mbar) (Fig. 5a), yielding almost the same I_{PPP}/I_{SSP} ratio (~20). Apparently, the orientation of CO molecules did not change in the studied pressure range.[33] Note that the peaks (2073–2076 cm^{-1}) were assigned to on-top CO adsorbed at stepped terraces, and there were only small changes in intensity and frequency, as at 300 K saturation is almost reached at 10^{-4} mbar. This agrees with previous results of CO on smooth Pt(111).[90] The observed increase of spectral intensity in PPP and SSP spectra can be attributed to the increasing surface coverage at a constant orientation angle.

At comparable CO pressure (e.g. 6 vs. 4 mbar), the signal of on-top CO on Pd(111) is several times weaker than that on Pt(111).[33] Thus, no quantitative orientation analysis can be obtained for CO on Pd(111) at 300 K, because the SSP spectra are too weak (even on-top CO PPP spectra are already quite weak in the entire pressure range of 10^{-6}–250 mbar; Fig. 5b).

Assuming CO is upright and based on the value of $I_{PPP}/I_{SSP} = 27$, the molecular hyperpolarizability ratio (R) of on-top CO on Pt(111) is deduced by simulation/modeling to be 0.49 (Fig. 5c),[33] approximately twice that of the free CO molecule ($R \approx 0.25$).[100] Or using $I_{PPP}/I_{SSP} = 27$, the tilt angles of on-top CO are 40°, 30°, 22° and 0° for R-values of 0.1, 0.3, 0.4 and 0.5, respectively.[33]
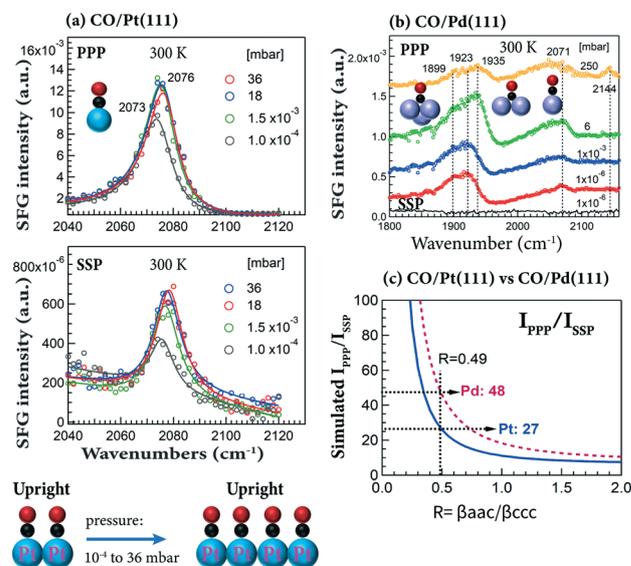

Fig. 5 Pressure-dependent PPP and SSP spectra at 300 K of (a) CO/Pt(111) and (b) CO/Pd(111). (c) Simulations of I_{PPP}/I_{SSP} vs. R for CO/Pt(111) and CO/Pd(111). Experimental configurations: $\alpha_{Vis} = 58.5°$ and $\alpha_{IR} = 55°$. Adapted from Li et al.[33] with permission from Springer.

18 | Catal. Sci. Technol., 2021, **11**, 12–26

This journal is © The Royal Society of Chemistry 2021

Similarly, at $\theta = 0°$ and $R = 0.49$, I_{PPP} is 48 times larger than I_{SSP} for CO on Pd(111) (Fig. 5c), indicating that SSP spectra are more difficult to measure on Pd(111) than on Pt(111).

Very recently, using the same experimental configuration (i.e. $\alpha_{Vis} = 58.5°$ and $\alpha_{IR} = 55°$), we also acquired the pressure- (and temperature-) dependent PPP and SSP spectra for CO adsorption on Ir(111).[32] Because PPP and SSP changed oppositely (Fig. 6a), i.e. I_{PPP}/I_{SSP} varied, this again indicated that the CO tilt angle changed with coverage. The CO tilt angle increases from 25° to 36° when the coverage increases from 0.62 to 0.77 ML (Fig. 6d), assuming $R = 0.08$.[32] Because the SSP signal was close to noise, CO on Ni(111) was reported to be upright (Fig. 6b and d). However, both PPP and SSP spectra with a relatively good signal-to-noise ratio were obtained for CO on NiO(111) (Fig. 6c), indicating that CO was (macroscopically) tilted.[47] This is due to the inclined trigonal NiO(111) microfacets, with CO adsorbing on the Ni^{2+} ions of the "slopes". Accordingly, the adsorbed CO molecules are oriented perpendicular to the NiO facets, but are tilted with respect to the underlying (111) surface (or the macroscopic surface normal) (Fig. 6d). Unfortunately, even though both PPP and SSP spectra of CO/NiO(111) were obtained, no quantitative analysis of tilt angles was performed.[47] On the (100) surfaces of body-centered cubic transition metals, DFT calculations also suggested CO to be tilted. For example, CO adsorbed molecularly at fourfold hollow sites with tilt angles respective to the surface normal of 47°, 57°, 57°, and 58° for Fe, Mo, Cr, and W, respectively. However, unlike having coverage-dependent tilt angles on Ir(111), no significant variation of the tilt angle of CO with coverage was found on these metal surfaces.[101]

As illustrated above, the SFG intensity depends on the incidence angles of laser beams, especially the visible beam. In ref. 47, relatively large incidence angles (~65°) of visible and IR beams (configuration1: $\alpha_{IR} = 65°$, $\alpha_{Vis} = 65°$) were

Fig. 7 Simulated (a) I_{PPP}, (b and c) I_{SSP} and (d) I_{PPP}/I_{SSP} as a function of α_{Vis} for CO on Ni(111) with $\alpha_{IR} = 65°$ and 55°. I_{PPP_1} and I_{SSP_1} were obtained at configuration1: α_{IR} and $\alpha_{Vis} = 65°$ (ref. 47); I_{PPP_2} and I_{SSP_2} were obtained at configuration2: $\alpha_{IR} = 55°$, $\alpha_{Vis} = 58.5°$ (ref. 32). Refractive indices of Ni: $n_2(Vis)^{102} = 1.88 + 3.49i$, $n_2(SFG)^{102} = 1.79 + 3.14i$, $n_2(IR)^{103} = 5.24 + 17.88i$; assumed $\beta_{ccc} = 1$, $\theta = 0°$, and $R = 0.08$ (determined by CO on Ir(111)[32]).

used, which are larger than those adapted in ref. 32 (configuration2: $\alpha_{IR} = 55°$, $\alpha_{Vis} = 58.5°$). Fig. 7 shows the simulated I_{PPP}, I_{SSP} and I_{PPP}/I_{SSP} vs. α_{Vis} with fixed $\alpha_{IR} = 55°$ and 65° for CO on Ni(111). I_{PPP_1} of configuration 1 is comparable to I_{PPP_2} of configuration 2. Both of I_{PPP_1} and I_{PPP_2} are nearly at maximum (Fig. 7a). Unfortunately, the I_{SSP_1} of configuration 1 and I_{SSP_2} of configuration 2 are quite small (Fig. 7b). However, I_{SSP_2} is still two times larger than I_{SSP_1} (Fig. 7c). When the α_{IR} had a 10° change (55° to 65°), the ratios of I_{PPP}/I_{SSP} were identical, but the I_{PPP}/I_{SSP} ratios strongly depended on α_{Vis}. When α_{Vis} increased from 58.5 to 65°, I_{PPP}/I_{SSP} increased from 1000 to 2200 (Fig. 7d). Therefore, the absence of the SSP signal for CO on Ni(111) in ref. 47 is likely caused by using a very large α_{Vis} (65°).

4.2 CO adsorption on supported metal nanoparticles

SFG has also been performed on supported Pd nanoparticles (grown by metal vapor deposition/electron beam evaporation on Al_2O_3 thin films) to bridge both the pressure and materials gaps.[29,30,81,89] The particle number density and size can be adjusted by accurately controlling the growth conditions. When the same Pd amount (nominal thickness of 0.4 nm) is deposited at 90 and 300 K, the particles are smaller (3.5 nm mean size) and less ordered (with more defects, edges, steps, etc.) and larger (6 nm mean size) and well-faceted, respectively.[81] For both sizes, under UHV conditions (10^{-7} mbar), the CO adsorption site occupancy on Pd nanoparticles was mainly governed by the particle surface structure,[89] but with the gas pressure (10^{-7}–200 mbar) controlling the coverage.[81] Typically, CO adsorbs on two different sites of the supported Pd nanoparticles: twofold bridging on particle edges and terraces and on-top at terraces and low-coordinated sites (Fig. 8). For the smaller "defective"

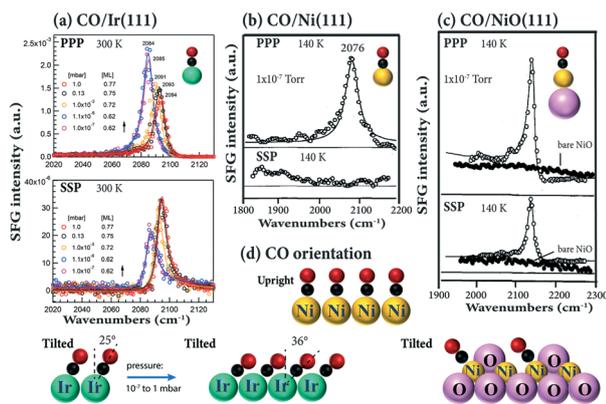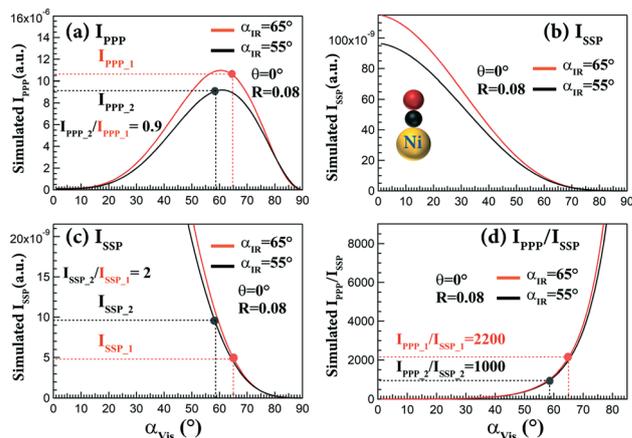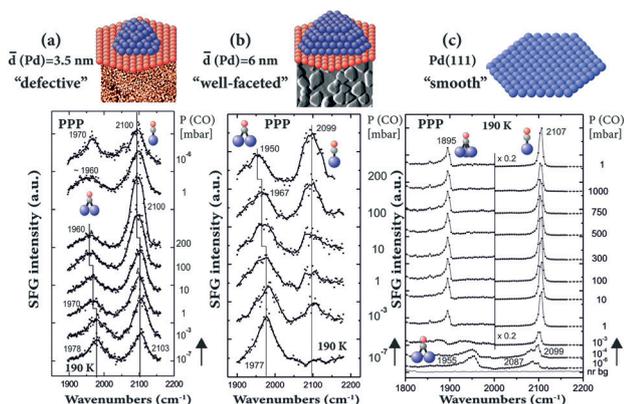
Fig. 6 (a) Pressure dependent PPP and SSP spectra of (a) CO/Ir(111) at 300 K. Experimental configurations: $\alpha_{IR} = 55°$, $\alpha_{Vis} = 58.5°$. Adapted from Li et al.[32] with permission. Copyright (2020) American Chemical Society. (b) CO/Ni(111) at 140 K. (c) CO/NiO(111) at 140 K. Experimental configurations of (b) and (c): $\alpha_{IR} = 65°$, $\alpha_{Vis} = 65°$, adapted from Bandara et al.[47] with permission from Elsevier.

This journal is © The Royal Society of Chemistry 2021

Catal. Sci. Technol., 2021, 11, 12–26 | 19

Fig. 8 Pressure-dependent PPP spectra at 190 K of CO on (a) 3.5 nm Pd/Al$_2$O$_3$/NiAl(110), (b) 6 nm Pd/Al$_2$O$_3$/NiAl(110) and (c) Pd(111). Adapted from Unterhalt *et al.*[89] with permission. Copyright (2002) American Chemical Society. Note that all spectra were acquired in PPP polarization combination.

NPs a higher fraction of on-top was observed (Fig. 8a), similar to rough Pd thin films.[65] For the larger "well-faceted" NPs (Fig. 8b), the on-top population was smaller at low pressure and the site occupancy compares best with the defect-rich (stepped or strongly sputtered) Pd(111),[89] rather than "smooth" Pd(111) (Fig. 8c). On Pd(111), a rearrangement of the (>0.5 ML) CO layer from a bridge (1955 cm^{-1})/on-top (2087 cm^{-1}) to a (~0.7 ML) hollow (1895 cm^{-1})/on-top (2107 cm^{-1}) configuration occurred at high pressure (≥1 mbar, Fig. 8c).[34]

It should be noted that the first SFG spectra of CO on supported nanoparticles (in Fig. 8 and ref. 29, 30 and 81) were obtained by using a Ti:Sa-based laser system. Although these spectra had a poor resolution of only approximately 25 cm^{-1} (Fig. 8a and b and 9c), they still provided valuable information about adsorbate structures on Pd nanoparticles. Using a Nd:YAG laser system (Fig. 9a and b), a clear improvement in resolution was obtained. Comparing the UHV spectra of CO adsorbed on 3.5 nm Pd nanoparticles acquired with Nd:YAG (Fig. 9b) and Ti:Sa (Fig. 9c) laser systems, not only the linewidth decreased, but also the
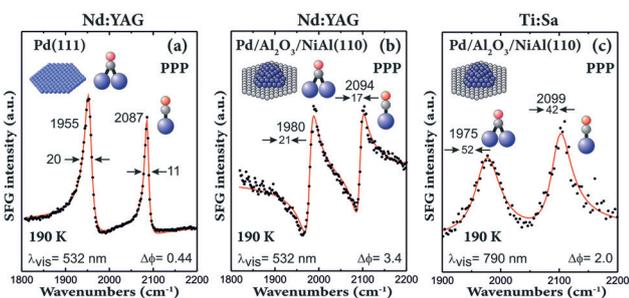
lineshape became very asymmetric. A similar linewidth was obtained for CO on Pd(111), but the peaks were more symmetric (Fig. 9a). The asymmetric lineshape observed on nanoparticles can thus be understood by the fact that the SFG signal originates from the interference between the resonant signal and the nonresonant background. For the Nd:YAG laser system, the nonresonant background was much higher for Pd nanoparticles than that for Pd(111), which is attributed to electric transitions in the NiAl(110) substrate.[104]

The adsorption of CO on 3.6 to 5.8 nm pyramidal Pd nanoparticles, grown on ultrathin MgO films on Ag(100), was studied at room temperature as a function of CO coverage by Bourguignon and coworkers (Fig. 10a and b),[105] and compared to CO on bulk Pd(100) (Fig. 10c).[36] For both Pd particle sizes, the spectroscopic signature was dominated by CO on the (100) top facets (~1880 to 1990 cm^{-1}), accompanied by few relatively weak bands at high coverage attributed to CO on (111) side facets, edges, and defects (>1930 cm^{-1} and 2040–2100 cm^{-1}). In both cases, the bridged CO peaks blue-shifted with higher coverage, from 1890 (low coverage; singleton frequency) to 1983 cm^{-1} (10^{-3} mbar) for smaller and larger NPs, respectively. Size-dependent spectra on Pd clusters and nanoparticles (4 to >500 atoms) on Al$_2$O$_3$/Ni$_3$Al(111) were reported in ref. 34.

In contrast, upon CO coverage increase on the Pd(100) single crystal, the SFG intensity first increased, but then decreased. This behavior is different from the "monotonic" increase of bridge bonded CO on Pd–MgO (Fig. 10a and b) and Pd(111) (Fig. 10d) and was explained by the coexistence of compressed and uncompressed CO (with the molecular hyperpolarizability at compressed sites being two times
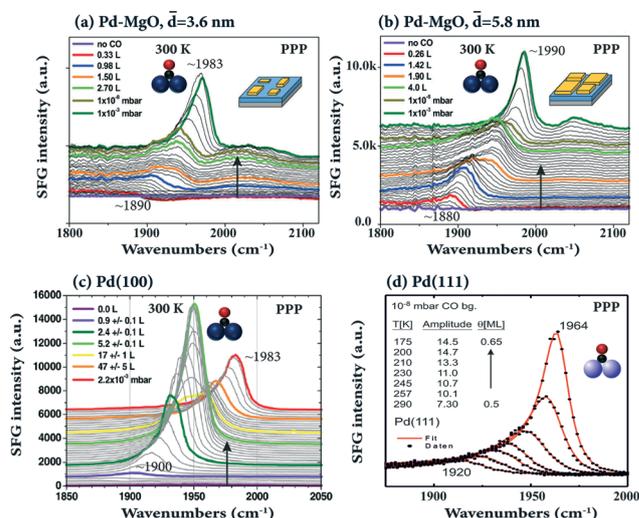

Fig. 9 SFG spectra of CO (near saturation coverage at 190 K) adsorbed on (a) Pd(111) and on (b and c) Pd/Al$_2$O$_3$/NiAl(110) with 3.5 nm Pd nanoparticles (grown at 90 K) acquired with Nd:YAG (a and b) and Ti:Sa (c) laser-based SFG spectrometers. Adapted from Morkel *et al.*[104] with permission from Elsevier. Note that all spectra were acquired in PPP polarization combination.

Fig. 10 SFG spectra of CO adsorbed on MgO-supported (a) 3.6 nm size and (b) 5.8 nm size Pd NPs at 300 K as a function of CO dose/pressure. Adapted from Ouvrard *et al.*[105] with permission. Copyright (2017) American Chemical Society. (c) CO on Pd(100) at 300 K, adapted from Ouvrard *et al.*[36] with permission. Copyright (2014) American Chemical Society. (d) CO on Pd(111) at the temperature range 175–290 K, adapted from Morkel *et al.*[104] with permission from Elsevier. Note that all spectra were acquired in PPP polarization combination.

20 | *Catal. Sci. Technol.*, 2021, **11**, 12–26

This journal is © The Royal Society of Chemistry 2021

smaller than at uncompressed sites). According to DFT compressed CO/Pd(100) is tilted by 8–9° with respect to the surface normal, but unfortunately, only PPP (no SSP) spectra were acquired in ref. 36.

Note that for CO/Pd(111) (Fig. 10d), there is a non-proportional relationship between the CO coverage and the SFG signal amplitude (coverage increases by ~30% from 0.5 to 0.65 ML, while the SFG amplitude doubles). The strong enhancement of the SFG amplitude may be due to coverage-dependent (increasing) Raman factors[99,104] or interference effects between different SFG susceptibility tensor elements.[45] A direct quantitative coverage analysis by integration of the SFG peak areas or *via* the amplitude is thus not possible.[89,106] Nevertheless, the strong coverage-dependence of the C–O stretching frequency, if known from combined TPD, XPS, LEED, IRAS or SFG UHV measurements, allows the actual CO coverage under mbar pressure conditions, *e.g.* for CO on Pd(111) or Ir(111), to be deduced.

The room temperature adsorption of CO on Pt clusters/nanoclusters, grown on a regular array template provided by the graphene/Ir(111) moiré structure, was examined by Vesselli and coworkers[107] by SFG, STM, XPS and DFT. SFG revealed adsorbate structures different from those on a Pt single crystal, on which only terminal CO was observed (*cf.* Fig. 3). On $Pt_{\sim 9}$ clusters, both bridge and on-top bonded CO species populate different sites of the clusters at terraces, borders, edges (Fig. 11a). For example, for $Pt_{\sim 9}$ CO at ~1870 cm^{-1} (Pt-bridge), ~1970–1995 cm^{-1} (on-top Pt at edges/corners), and ~2040–2060 cm^{-1} (on-top Pt at borders and 1st layer terraces) appeared. For larger Pt nanoparticles, typical on-top CO on terraces was observed (~2070–2105 cm^{-1}).

Furthermore, upon CO adsorption a significant restructuring of the Pt clusters was observed, promoting particle sintering for small clusters and reshaping for large ones (similar CO-induced restructuring/mobility was reported for Pt nanoparticles[108] and

Cu clusters[109]). Above 420 K at 0.1 mbar, there was CO spillover from Pt clusters to the underlying graphene/Ir(111) interface (*i.e.* intercalated CO at 2060–2080 cm^{-1} ref. 32 and 98) promoted by the Pt particles. Once more, SFG has been successfully used to reveal CO adsorption sites on the surface of nanoparticles, but due to the lack of SSP spectra, there is unfortunately no information about the CO orientation. *Vice versa*, using high-resolution broadband SFG, Ren and coworkers[110] reported SSP (but no PPP) spectra of CO adsorption on z-cut α-quartz-supported Pt nanoparticles at 1 bar.

The adsorption of ~1 bar CO on Pt nanoparticle arrays on SiO_2, with polycrystalline Pt particles grown by electron beam lithography (30, 40, 45, 200, and 1000 nm in mean size),[29,111–113] was reported by Baldelli *et al.*[114] On-top CO was characterized both in PPP and SSP polarization combinations (Fig. 11b) and a strong signal enhancement was attributed to the surface plasmon resonance in the 45 nm Pt particles and the dielectric properties of the SiO_2 substrate (but no CO orientation information was provided).

4.3 Isotopic CO adsorption on single crystals and Pd nanoparticles

The adsorption of CO on metal surfaces has been widely used to characterize the available surface adsorption sites. With increasing coverage, the adsorbate–adsorbate interactions can be described by vibrational (dipole–dipole) coupling and by chemical (through substrate) interaction.[65] These two effects can be disentangled by isotopic mixtures, as the vibrational frequencies of $^{12}C^{16}O$ and $^{12}C^{18}O$ (or $^{13}C^{18}O$) are too different to enable dipole-coupling.

The adsorbate–metal and adsorbate–adsorbate interactions determine the frequency and intensity of the vibrational bands.[95] An abnormal coverage dependence was observed for CO on Ni(111). At low coverage (0.04–0.4 ML) CO preferred to adsorb on the bridge sites of Ni(111), but as the coverage further increased (0.47 ML), the signal of bridge CO weakened upon appearance of on-top CO and finally disappeared at 0.60 ML. To examine the possibility that the bridge bonded CO did not really weaken/disappear, but was rather screened by the high-frequency dipoles of on-top CO, the adsorption of isotopic mixtures was studied: $^{12}C^{16}O$ and $^{12}C^{18}O$ on Ni(111) at 0.33 ML with only bridge CO on the surface, and at 1 ML with only on-top CO on the surface (Fig. 12a). Note that as the $^{12}C^{16}O$ concentration decreased, the signal of bridge $^{12}C^{16}O$ (1920 cm^{-1}) and on-top $^{12}C^{16}O$ (2074 cm^{-1}) monotonically decreased, and the signal of bridge $^{12}C^{18}O$ (1890 cm^{-1}) and on-top $^{12}C^{18}O$ (2022 cm^{-1}) monotonically increased, suggesting that the intensity transfer between the $^{12}C^{16}O$ and $^{12}C^{18}O$ bands is not sufficient to suppress one of the two peaks. Rather than the screening of the bridged CO band by on-top CO, a change in the Raman tensor is thus responsible for the disappearance of bridge CO at high coverage.[95]

Furthermore, isotopic experiments help to understand coverage-dependent changes in the CO stretch frequency. Fig. 12b shows three SFG spectra of isotopic $^{12}C^{16}O/^{13}C^{18}O$
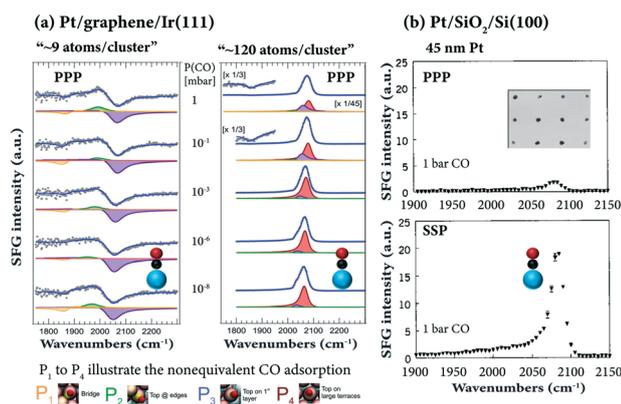

Fig. 11 SFG spectra of CO adsorbed on supported Pt: (a) CO at 10^{-8}–1 mbar at 300 K on Pt nanoclusters grown on graphene/Ir(111), adapted from Podda *et al.*[107] with permission. Copyright (2017) American Chemical Society. (b) CO at 1 bar at 300 K on polycrystalline Pt particles (45 nm size) grown by electron beam lithography, adapted from Baldelli *et al.*[114] with permission. Copyright (2000) American Institute of Physics.
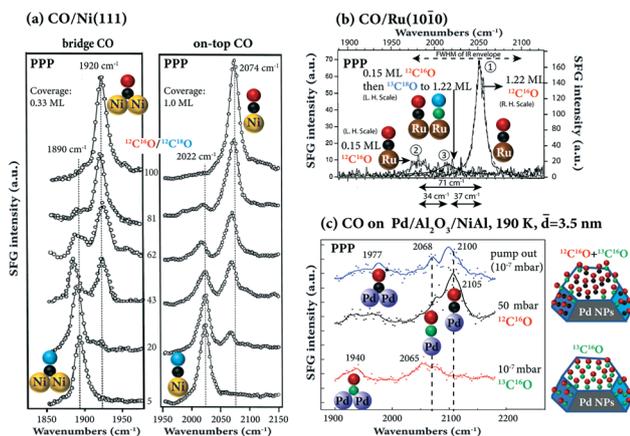
Fig. 12 (a) Isotopic $^{12}C^{16}O$ and $^{12}C^{18}O$ adsorption on Ni(111). The ratio of $^{12}C^{16}O$ and $^{12}C^{18}O$ was determined by the TPD peak area. Adapted from Bandara et al.[95] with permission from Elsevier. (b) Isotope $^{12}C^{16}O$ and $^{13}C^{18}O$ adsorption on Ru(10$\bar{1}$0), adapted from Symonds et al.[115] with permission. Copyright (2004) American Institute of Physics. (c) Isotope $^{12}C^{16}O$ and $^{13}C^{16}O$ adsorption on Pd/Al$_2$O$_3$/NiAl(110), adapted from Unterhalt et al.[89] with permission. Copyright (2002) American Chemical Society. Note that all spectra were acquired in PPP polarization combination.

adsorption on Ru(10$\bar{1}$0) in PPP polarization combination. The first was acquired at saturation coverage of $^{12}C^{16}O$. Then, for comparison a spectrum at 0.15 ML coverage of $^{12}C^{16}O$ was taken. Apparently, there is a total frequency shift of 71 cm^{-1}, due to the combined contributions of dipole–dipole coupling and chemical shift. Then, the 0.15 ML $^{12}C^{16}O$ surface was filled with $^{13}C^{18}O$ up to saturation coverage and a third spectrum was measured. Since the $^{12}C^{16}O$ molecules do not couple well to the heavier $^{13}C^{18}O$ molecules, the observed 34 cm^{-1}-shift is largely chemical in nature. Apparently, the effects of dipole coupling and chemical shift on the CO frequency shift can be quantitatively disentangled. Unfortunately, only PPP spectra were recorded. The orientation information of CO on Ru(10$\bar{1}$0) as well as isotopic effects on the CO orientation angle remains unclear. Similarly, the adsorption of an isotopic mixture of $^{12}C^{16}O$ and $^{13}C^{16}O$ on Al$_2$O$_3$-supported Pd nanoparticles has been studied by SFG,[89] revealing high mobility of the adsorbed CO molecules at 190 K. As shown in Fig. 12c, Pd particles of 3.5 nm mean size were saturated with $^{13}C^{16}O$ resulting in a bridge and an on-top peak at lower wavenumbers (1940 and 2065 cm^{-1}) due to the isotopic effect. When the sample was exposed to 50 mbar of $^{12}C^{16}O$, the on-top peak was shifted to 2105 cm^{-1} (the resonance frequency of $^{12}C^{16}O$), indicating exchange of molecules. However, the exchange was not complete because a shoulder of linear $^{13}C^{16}O$ (~2068 cm^{-1}) still existed. The remaining linear $^{13}C^{16}O$ may be bonded to defects or edges. When the CO gas was pumped out, the spectrum exhibited peaks originating from linearly bonded $^{12}C^{16}O$ (2100 cm^{-1}) and $^{13}C^{16}O$ (2068 cm^{-1}) and a broad bridge peak with a maximum around 1977 cm^{-1}. Once more, without SSP spectra, orientation angles of the strongly bound

$^{13}C^{16}O$ (not exchanged with $^{12}C^{16}O$) and the on-top $^{12}C^{16}O$ cannot be determined.

4.4 SFG under reaction conditions

One of the main benefits of SFG spectroscopy is that it can be performed during an ongoing catalytic reaction (in situ or operando), such as CO oxidation on Pt(111),[37] on Pt nanoparticles supported on ZrO$_2$,[28] and on Rh(111),[84] or CO hydrogenation on Pd(111),[89,116,117] and methanol oxidation on Pd nanoparticles supported on Al$_2$O$_3$.[118]

Some examples of SFG spectra recorded during CO oxidation and hydrogenation are depicted in Fig. 13. For CO oxidation (CO/O$_2$ = 1 : 2) on ZrO$_2$-supported Pt nanoparticles at 523 K (Fig. 13a), an intense on-top CO peak was observed at 2085 cm^{-1}, and only little CO$_2$ was generated since the Pt surface was CO poisoned. Upon increasing the temperature, an increase in CO$_2$ was observed and at 623 K the conversion of CO and O$_2$ was at maximum. At this temperature, even though the SFG spectra decreased in intensity and red-shifted in frequency (shifted from 2085 to 2077 cm^{-1}) which indicated a decreasing CO coverage, some facets of Pt nanoparticles were still covered by CO due to the strong on-top CO peak in the SFG spectra. Therefore, CO$_2$-production occurred at non-poisoned sites of Pt nanoparticles (defects or metal/oxide interfaces). For CO oxidation on polycrystalline Pt foil, the order of the ignition temperatures is (110) < (100) < (111), in line with a facet-dependent stepwise lifting of CO poisoning.[119]

A lower (~450 K) ignition temperature was found for the CO oxidation (CO/O$_2$ = 1 : 2) on Rh(111).[84] As shown in Fig. 13b, below 400 K the presence of O$_2$ in the stagnation
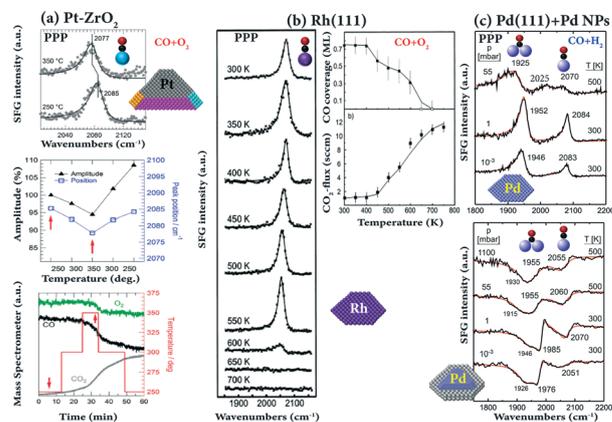

Fig. 13 SFG and MS spectra of CO oxidation on (a) Pt–ZrO$_2$ at 10 mbar CO and 20 mbar O$_2$; Pt particles of 7 nm size on a ZrO$_2$ film of 42 nm thickness; adapted from Roiaz et al.[28] with permission. Copyright (2018) American Institute of Physics. (b) Rh(111) under laminar flow conditions at a total pressure of 20 mbar in a stagnation point flow (CO, 15 sccm; O$_2$, 30 sccm; Ar, 105 sccm; flow velocity 2.5 cm s^{-1}), adapted from Pery et al.[84] with permission from Elsevier. (c) CO hydrogenation (CO/H$_2$ = 1 : 10) on Pd(111) and Pd/Al$_2$O$_3$/NiAl(110). Pressures and temperatures are indicated, adapted from Morkel et al.[117] with permission from Elsevier. All spectra were measured in PPP polarization combination.

flow did not result in a reduction of the CO coverage, indicating that adsorbed CO efficiently blocked the adsorption of oxygen. At 450 K, the CO coverage apparently decreases and the onset of CO_2 production is noted. In the temperature range 400–600 K, not only the CO coverage linearly decreased, but also the CO frequency gradually redshifted. The sudden decrease in CO coverage above 600 K was a result of a transition from a predominately CO-covered surface state to an O-covered state, originating from an increase of dissociative oxygen adsorption upon decreasing CO coverage and the increase of the surface reaction rate. Further post-reaction AES spectra revealed that only trace amounts of surface carbon and Rh surface oxides were formed upon CO oxidation under the investigated conditions.

For CO oxidation on polycrystalline Rh foil, defect-rich (high Miller-index) Rh surfaces appeared to be much more tolerant towards CO poisoning than annealed (smooth) surfaces. Nanometer-sized Rh nanotips, representing Rh NPs, were found to be even more CO tolerant.[120]

Additionally, CO/H_2 coadsorption and CO hydrogenation on Pd(111) were studied by SFG, showing that the adsorption site occupancy depended on the type of gas exposure (sequential dosing *vs.* co-dosing). When Pd(111) was exposed to 1:1 CO/H_2 mixtures under UHV at 100 K, on-top CO was absent due to hydrogen atoms diffusing between hollow sites *via* bridge sites that destabilized neighboring on-top CO molecules. Preadsorbed surface hydrogen prevented CO adsorption at 100 K, but it was replaced by CO above 125 K and H_2 desorption started only after a considerable amount of CO had desorbed.

To monitor the CO–H reaction at high temperature, SFG experiments of a 1:10 CO/H_2 mixture on Pd(111) and on Pd/Al_2O_3/NiAl(110) were carried out at elevated pressure (Fig. 13c). On Pd(111) at 500 K, a peak at 1925 cm^{-1} (bridge CO) was accompanied by weak features (on-top CO) at ~2025 cm^{-1} and ~2070 cm^{-1} at 55 mbar, while for low temperature (UHV) CO spectra a bridge (or hollow) bonded CO signal around 1925 cm^{-1} did not occur in combination with on-top CO.[89] Consequently, the species at 2070 cm^{-1} and 2025 cm^{-1} may indicate that the Pd(111) surface is (partially) roughened under reaction conditions.

Similar to CO/H_2 on Pd(111), at high pressure (55 mbar) and at high temperature (500 K), a modified adsorbate structure was also observed for Pd/Al_2O_3 where a bridging species at 1955 cm^{-1} was accompanied by an on-top feature around 2060 cm^{-1} (Fig. 13c). Such a low-frequency on-top CO species does not occur under UHV[121] and again points to a possible surface roughening. Unfortunately, only trace amounts of CO hydrogenation products (methanol or methane) were detected by gas chromatographic and mass spectroscopic detection[117] due to the small turnover frequency of Pd (~5 × 10^{-4} s^{-1} at 550 K)[122] and the small Pd surface area of the model catalysts.

adsorption and reaction of (isotopic) CO on single crystals and supported nanoparticles over wide pressure ranges (from UHV to atmospheric) and over wide temperature ranges (from 90 to 700 K). The aim of such investigations is to analyse adsorbate sites and geometries, molecular orientation (and changes thereof) of CO on different (low-index) single crystals and (oxide- or graphene-supported) nanoparticles, as a function of CO gas pressure and/or substrate temperature, approaching technological reaction conditions.

The adsorbate geometries that were observed on the (111) facets of platinum, rhodium, iridium, and copper single crystals are similar, with on-top CO dominating the SFG spectra. No high-pressure species were observed, but coverage is apparently controlled by pressure and temperature. The site population cannot be extrapolated from UHV studies, especially when the population of hollow, bridge and on-top CO sensitively depends on coverage, *e.g.* on Pd(111). Different from the known adsorbate geometries, the coverage-dependent molecular orientation (tilt angle) of CO on most single crystals is still lacking (and thus typically considered to be upright and constant). So far, only the orientation analysis of CO on Pt(111) and Ir(111) was performed by SFG, as for these systems spectra both in PPP and SSP polarizations were obtained simultaneously. The orientation angle of CO on Pt(111) was found to be independent of coverage, whereas for CO on Ir(111) it is coverage-dependent (*i.e.* CO is upright at low coverage, but tilted at high coverage). In addition, assuming upright CO, the hyperpolarizability ratios of CO on Pt(111) and on Ir(111) were deduced to be 0.49 and 0.08, respectively. For CO adsorption on supported metal nanoparticles, the adsorbate geometries are typically different from those obtained on single crystals, because nanoparticles exhibit several different facets and edges/defects. Using isotopically labelled CO allows dynamic and static coupling to be disentangled. SFG spectroscopy under reaction conditions revealed that CO_2-production may start at defects or metal/oxide interfaces of CO-covered Pt nanoparticles. The onset temperature of CO_2 production on Rh(111) is above 400 K, and only trace amounts of surface carbon and Rh surface oxides were formed upon CO oxidation. Under high pressure and at high temperature, both Pd(111) and Pd/Al_2O_3 surfaces were (partially) roughened in the CO/H_2 mixture, but only minute amounts of CO hydrogenation products were detected. The continued combined application of model catalysts and polarization-dependent SFG spectroscopy, especially under *operando* conditions with simultaneous SFG/MS analysis, will thus improve our understanding of catalytic processes in heterogeneous catalysis.

5. Conclusions

The few case studies presented illustrate how vibrational SFG spectroscopy can be applied to characterize the

Conflicts of interest

There are no conflicts of interest to declare.

This journal is © The Royal Society of Chemistry 2021

Catal. Sci. Technol., 2021, **11**, 12–26 | **23**

Acknowledgements

References

1 G. A. Somorjai and Y. M. Li, *Introduction to Surface Chemistry and Catalysis*, Wiley-VCH Verlag GmbH & Co. KGaA, 2010.

2 G. Ertl, *Angew. Chem., Int. Ed.*, 2008, **47**, 3524–3535.

3 G. A. Somorjai and G. Rupprechter, *J. Chem. Educ.*, 1998, **75**, 161–176.

4 G. Ertl and H.-J. Freund, *Phys. Today*, 1999, **52**, 32–38.

5 J. Sauer and H.-J. Freund, *Catal. Lett.*, 2015, **145**, 109–125.

6 G. Rupprechter, in *Advances in Catalysis*, ed. B. Gates and H. Knözinger, Academic, New York, 2007, vol. 51, pp. 133–263.

7 G. Rupprechter, *Annu. Rep. Prog. Chem., Sect. C: Phys. Chem.*, 2004, **100**, 237–311.

8 C. T. Campbell, *Surf. Sci. Rep.*, 1997, **27**, 1–111.

9 A. Ghalgaoui and M. Sterrer, *J. Phys. Chem. C*, 2020, **124**, 4190–4195.

10 Y. J. Tong, F. Lapointe, M. Thamer, M. Wolf and R. K. Campen, *Angew. Chem., Int. Ed.*, 2017, **56**, 4211–4214.

11 H. Tatsumi, F. D. Liu, H. L. Han, L. M. Carl, A. Sapi and G. A. Somorjai, *J. Phys. Chem. C*, 2017, **121**, 7365–7371.

12 X. Li and G. Rupprechter, *Chin. J. Catal.*, 2019, **40**, 1655–1667.

13 I. V. Yudanov, R. Sahnoun, K. M. Neyman, N. Rösch, J. Hoffmann, S. Schauermann, V. Johánek, H. Unterhalt, G. Rupprechter, J. Libuda and H.-J. Freund, *J. Phys. Chem. B*, 2003, **107**, 255–264.

14 H.-J. Freund and G. Pacchioni, *Chem. Soc. Rev.*, 2008, **37**, 2224–2242.

15 G. Pacchioni, *ChemPhysChem*, 2003, **4**, 1041–1047.

16 V. K. Markova, J. P. Philbin, W. Zhao, A. Genest, J. Silvestre-Albero, G. Rupprechter and N. Rösch, *ACS Catal.*, 2018, **8**, 5675–5685.

17 C. Spiel, P. Blaha, Y. Suchorski, K. Schwarz and G. Rupprechter, *Phys. Rev. B: Condens. Matter Mater. Phys.*, 2011, **84**, 045412.

18 L. Moskaleva, C. C. Chiu, A. Genest and N. Rosch, *Chem. Rec.*, 2016, **16**, 2388–2404.

19 R. A. Vansanten and M. Neurock, *Catal. Rev.: Sci. Eng.*, 1995, **37**, 557–698.

20 M. V. Ganduglia-Pirovano, A. Hofmann and J. Sauer, *Surf. Sci. Rep.*, 2007, **62**, 219–270.

21 M. Morkel, H. Unterhalt, M. Salmeron, G. Rupprechter and H.-J. Freund, *Surf. Sci.*, 2003, **532**, 103–107.

22 W. Reichl, G. Rosina, G. Rupprechter, C. Zimmermann and K. Hayek, *Rev. Sci. Instrum.*, 2000, **71**, 1495–1499.

23 G. A. Somorjai, *Chem. Rev.*, 1996, **96**, 1223–1235.

24 J. Szanyi and D. W. Goodman, *Rev. Sci. Instrum.*, 1993, **64**, 2350–2352.

25 D. Godbey, F. Zaera, R. Yeates and G. A. Somorjai, *Surf. Sci.*, 1986, **167**, 150–166.

26 A. L. Cabrera, N. D. Spencer, E. Kozak, P. W. Davies and G. A. Somorjai, *Rev. Sci. Instrum.*, 1982, **53**, 1888–1893.

27 D. W. Blakely, E. I. Kozak, B. A. Sexton and G. A. Somorjai, *J. Vac. Sci. Technol.*, 1976, **13**, 1091–1096.

28 M. Roiaz, V. Pramhaas, X. Li, C. Rameshan and G. Rupprechter, *Rev. Sci. Instrum.*, 2018, **89**, 045104.

29 G. Rupprechter and H.-J. Freund, *Top. Catal.*, 2001, **14**, 3–14.

30 G. Rupprechter, *Phys. Chem. Chem. Phys.*, 2001, **3**, 4621–4632.

31 Y. R. Shen, *Nature*, 1989, **337**, 519–525.

32 X. Li, V. Pramhaas, C. Rameshan, P. Blaha and G. Rupprechter, *J. Phys. Chem. C*, 2020, **124**, 18102–18111.

33 X. Li, M. Roiaz, V. Pramhaas, C. Rameshan and G. Rupprechter, *Top. Catal.*, 2018, **61**, 751–762.

34 N. Alyabyeva, A. Ouvrard, A.-M. Zakaria and B. Bourguignon, *J. Phys. Chem. Lett.*, 2019, **10**, 624–629.

35 G. Rupprechter, *MRS Bull.*, 2007, **32**, 1031–1037.

36 A. Ouvrard, J. J. Wang, A. Ghalgaoui, S. Nave, S. Carrez, W. Q. Zheng, H. Dubost and B. Bourguignon, *J. Phys. Chem. C*, 2014, **118**, 19688–19700.

37 G. A. Somorjai and G. Rupprechter, *J. Phys. Chem. B*, 1999, **103**, 1623–1638.

38 X. C. Su, P. S. Cremer, Y. R. Shen and G. A. Somorjai, *Phys. Rev. Lett.*, 1996, **77**, 3858–3860.

39 C. T. Williams, Y. Yang and C. D. Bain, *Catal. Lett.*, 1999, **61**, 7–13.

40 G. A. Somorjai, *Surf. Sci.*, 1995, **335**, 10–22.

41 P. S. Cremer, X. C. Su, Y. R. Shen and G. A. Somorjai, *J. Am. Chem. Soc.*, 1996, **118**, 2942–2949.

42 P. S. Cremer, X. C. Su, Y. R. Shen and G. A. Somorjai, *Catal. Lett.*, 1996, **40**, 143–145.

43 P. S. Cremer, B. J. McIntyre, M. Salmeron, Y. R. Shen and G. A. Somorjai, *Catal. Lett.*, 1995, **34**, 11–18.

44 P. Cremer, C. Stanners, J. W. Niemantsverdriet, Y. R. Shen and G. Somorjai, *Surf. Sci.*, 1995, **328**, 111–118.

45 S. Baldelli, N. Markovic, P. Ross, Y. R. Shen and G. Somorjai, *J. Phys. Chem. B*, 1999, **103**, 8920–8925.

46 M. Fang, G. Santos, X. L. Chen and S. Baldelli, *Surf. Sci.*, 2016, **648**, 35–41.

47 A. Bandara, S. Dobashi, J. Kubota, K. Onda, A. Wada, K. Domen, C. Hirose and S. S. Kano, *Surf. Sci.*, 1997, **387**, 312–319.

48 C. T. Williams and D. A. Beattie, *Surf. Sci.*, 2002, **500**, 545–576.

49 S. B. Waldrup and C. T. Williams, *Catal. Commun.*, 2007, **8**, 1373–1376.

50 M. S. Yeganeh, S. M. Dougal and B. G. Silbernagel, *Langmuir*, 2006, **22**, 637–641.

51 S. J. Kweskin, R. M. Rioux, S. E. Habas, K. Komvopoulos, P. Yang and G. A. Somorjai, *J. Phys. Chem. B*, 2006, **110**, 15920–15925.

52 G. Kennedy, L. R. Baker and G. A. Somorjai, *Angew. Chem., Int. Ed.*, 2014, **53**, 3405–3408.

53 G. Tourillon, L. Dreesen, C. Volcke, Y. Sartenaer, P. A. Thiry and A. Peremans, *Nanotechnology*, 2007, **18**, 415301.

54 M. Salmeron and R. Schlögl, *Surf. Sci. Rep.*, 2008, **63**, 169–199.

55 X. Zhou, F. Bebensee, M. Yang, R. Bebensee, F. Cheng, Y. He, Q. Shen, J. Shang, Z. Liu, F. Besenbacher, T. R. Linderoth and K. Wu, *ACS Nano*, 2017, **11**, 9397–9404.

56 W. de Poel, S. J. T. Brugman, K. H. A. van de Ven, A. Gasseling, J. de Lange, E. R. Townsend, A. H. J. Engwerda, M. Jankowski, M. A. R. Blijlevens, B. Werkhoven, J. Drnec, F. Carla, R. Felici, A. Tuladhar, N. M. Adhikari, J. J. De Yoreo, J. A. A. W. Elemans, W. J. P. van Enckevort, A. E. Rowan and E. Vlieg, *Angew. Chem., Int. Ed.*, 2020, **59**, 2323–2327.

57 E. Arakawa, in *Compendium of Surface and Interface Analysis*, ed. The Surface Science Society of Japan, Springer, Singapore, 2018, pp. 689–696.

58 M. Plodinec, H. C. Nerl, F. Girgsdies, R. Schlögl and T. Lunkenbein, *ACS Catal.*, 2020, **10**, 3183–3193.

59 J. V. Lauritsen and F. Besenbacher, *J. Catal.*, 2015, **328**, 49–58.

60 J. Frenken and I. Groot, *Operando Research in Heterogeneous Catalysis*, Springer, Switzerland, 2017.

61 J. Dou, Z. Sun, A. A. Opalade, N. Wang, W. Fu and F. Tao, *Chem. Soc. Rev.*, 2017, **46**, 2001–2027.

62 G. Rupprechter, in *Surface and Interface Science*, ed. K. Wandelt, Wiey-VCH Verlag GmbH & Co. KGaA, Germany, 2016, pp. 459–528.

63 K. Föttinger and G. Rupprechter, *Acc. Chem. Res.*, 2014, **47**, 3071–3079.

64 J. H. Hunt, P. Guyotsionnest and Y. R. Shen, *Chem. Phys. Lett.*, 1987, **133**, 189–192.

65 F. M. Hoffmann, *Surf. Sci. Rep.*, 1983, **3**, 107–192.

66 P. Miranda and Y. Shen, *J. Phys. Chem. B*, 1999, **103**, 3292–3307.

67 C. Hirose, N. Akamatsu and K. Domen, *Appl. Spectrosc.*, 1992, **46**, 1051–1072.

68 H. F. Wang, W. Gan, R. Lu, Y. Rao and B. H. Wu, *Int. Rev. Phys. Chem.*, 2005, **24**, 191–256.

69 G. Rupprechter and A. Bandara, in *Surface and Thin Film Analysis: A compendium of Principles, Instrumentation, and Applications*, ed. G. Friedbacher and H. Bubert, Wiey-VCH Verlag GmbH & Co. KGaA, Germany, 2011, pp. 407–435.

70 W. Liu, L. Fu, Z. G. Wang, Z. Sohrabpour, X. B. Li, Y. T. Liu, H. F. Wang and E. C. Y. Yan, *Phys. Chem. Chem. Phys.*, 2018, **20**, 22421–22426.

71 X. Li, G. Z. Deng, L. Ma and X. L. Lu, *Langmuir*, 2018, **34**, 9453–9459.

72 T. Iwahashi, T. Ishiyama, Y. Sakai, A. Morita, D. Kim and Y. Ouchi, *Phys. Chem. Chem. Phys.*, 2015, **17**, 24587–24597.

73 T. Iwahashi, T. Miyamae, K. Kanai, K. Seki, D. Kim and Y. Ouchi, *ACS Symp. Ser. Am. Chem. Soc.*, 2009, **1030**, 305–316.

74 M. M. Knock, G. R. Bell, E. K. Hill, H. J. Turner and C. D. Bain, *J. Phys. Chem. B*, 2003, **107**, 10801–10814.

75 L. F. Scatena and G. L. Richmond, *J. Phys. Chem. B*, 2001, **105**, 11240–11250.

76 L. F. Scatena, M. G. Brown and G. L. Richmond, *Science*, 2001, **292**, 908–912.

77 J. C. Conboy, M. C. Messmer and G. L. Richmond, *J. Phys. Chem.*, 1996, **100**, 7617–7622.

78 M. C. Messmer, J. C. Conboy and G. L. Richmond, *J. Am. Chem. Soc.*, 1995, **117**, 8039–8040.

79 G. Mizutani and Y. Miyauchi, *Surf. Interface Anal.*, 2010, **42**, 1675–1679.

80 Y. Miyauchi, H. Sano, J. Okada, H. Yamashita and G. Mizutani, *Surf. Interface Anal.*, 2010, **42**, 1667–1670.

81 T. Dellwig, G. Rupprechter, H. Unterhalt and H.-J. Freund, *Phys. Rev. Lett.*, 2000, **85**, 776–779.

82 C. Klünker, M. Balden, S. Lehwald and W. Daum, *Surf. Sci.*, 1996, **360**, 104–111.

83 E. Carrasco, A. Aumer, M. A. Brown, R. Dowler, I. Palacio, S. Song and M. Sterrer, *Surf. Sci.*, 2010, **604**, 1320–1325.

84 T. Pery, M. G. Schweitzer, H. R. Volpp, J. Wolfrum, L. Ciossu, O. Deutschmann and J. Warnatz, *Proc. Combust. Inst.*, 2002, **29**, 973–980.

85 I. M. Lane, D. A. King and H. Arnolds, *J. Chem. Phys.*, 2007, **126**, 024707.

86 J. C. Owrutsky, J. P. Culver, M. Li, Y. R. Kim, M. J. Sarisky, M. S. Yeganeh, A. G. Yodh and R. M. Hochstrasser, *J. Chem. Phys.*, 1992, **97**, 4421–4427.

87 M. Corva, M. Rinaldi, Z. Feng, M. Roiaz, C. Rameshan, G. Rupprechter, R. Costantini, M. Dell'Angela, G. Pastore, G. Comelli, N. Seriani and E. Vesselli, *Nat. Commun.*, 2018, **9**, 4703.

88 K. Y. Kung, P. Chen, F. Wei, Y. R. Shen and G. A. Somorjai, *Surf. Sci.*, 2000, **463**, L627–L633.

89 H. Unterhalt, G. Rupprechter and H.-J. Freund, *J. Phys. Chem. B*, 2002, **106**, 356–367.

90 G. Rupprechter, T. Dellwig, H. Unterhalt and H.-J. Freund, *J. Phys. Chem. B*, 2001, **105**, 3797–3802.

91 S. Westerberg, C. Wang and G. A. Somorjai, *Surf. Sci.*, 2005, **582**, 137–144.

92 J. Lauterbach, R. W. Boyle, M. Schick, W. J. Mitchell, B. Meng and W. H. Weinberg, *Surf. Sci.*, 1996, **350**, 32–44.

93 C. M. Comrie and W. H. Weinberg, *J. Chem. Phys.*, 1976, **64**, 250–259.

94 H. Härle, A. Lehnert, U. Metka, H. R. Volpp, L. Willms and J. Wolfrum, *Appl. Phys. B: Lasers Opt.*, 1999, **68**, 567–572.

95 A. Bandara, S. Katano, J. Kubota, K. Onda, A. Wada, K. Domen and C. Hirose, *Chem. Phys. Lett.*, 1998, **290**, 261–267.

96 G. A. Somorjai, *Surf. Sci.*, 2006, **600**, 240–240.

97 C. Gutierrez, *Surf. Sci.*, 2005, **595**, 249–251.

98 M. Corva, Z. J. Feng, C. Dri, F. Salvador, P. Bertoch, G. Comelli and E. Vesselli, *Phys. Chem. Chem. Phys.*, 2016, **18**, 6763–6772.

99 P. Galletto, H. Unterhalt and G. Rupprechter, *Chem. Phys. Lett.*, 2003, **367**, 785–790.

100 S. J. A. van Gisbergen, J. G. Snijders and E. J. Baerends, *J. Chem. Phys.*, 1998, **109**, 10657–10668.

This journal is © The Royal Society of Chemistry 2021

Catal. Sci. Technol., 2021, **11**, 12–26 | **25**

101 F. J. E. Scheijen, D. C. Ferre and J. W. Niemantsverdriet, *J. Phys. Chem. C*, 2009, **113**, 11041–11049.

102 P. B. Johnson and R. W. Christy, *Phys. Rev. B: Solid State*, 1974, **9**, 5056–5070.

103 M. A. Ordal, R. J. Bell, R. W. Alexander, L. L. Long and M. R. Querry, *Appl. Opt.*, 1987, **26**, 744–752.

104 M. Morkel, H. Unterhalt, T. Klüner, G. Rupprechter and H.-J. Freund, *Surf. Sci.*, 2005, **586**, 146–156.

105 A. Ouvrard, A. Ghalgaoui, C. Michel, C. Barth, J. J. Wang, S. Carrez, W. Q. Zheng, C. R. Henry and B. Bourguignon, *J. Phys. Chem. C*, 2017, **121**, 5551–5564.

106 G. Rupprechter, H. Unterhalt, M. Morkel, P. Galletto, L. J. Hu and H.-J. Freund, *Surf. Sci.*, 2002, **502**, 109–122.

107 N. Podda, M. Corva, F. Mohamed, Z. J. Feng, C. Dri, F. Dvorak, V. Matolin, G. Comelli, M. Peressi and E. Vesselli, *ACS Nano*, 2017, **11**, 1041–1053.

108 A. Haghofer, P. Sonström, D. Fenske, K. Föttinger, S. Schwarz, J. Bernardi, K. Al-Shamery, M. Bäumer and G. Rupprechter, *Langmuir*, 2010, **26**, 16330–16338.

109 M. Roiaz, L. Falivene, C. Rameshan, L. Cavallo, S. M. Kozlov and G. Rupprechter, *J. Phys. Chem. C*, 2019, **123**, 8112–8121.

110 T. Luo, R. D. Zhang, X. X. Peng, X. T. Liu, C. Y. Zhou, X. M. Yang and Z. F. Ren, *Surf. Sci.*, 2019, **689**, 121459.

111 A. S. Eppler, G. Rupprechter, L. Guczi and G. A. Somorjai, *J. Phys. Chem. B*, 1997, **101**, 9973–9977.

112 A. Avoyan, G. Rupprechter, A. S. Eppler and G. A. Somorjai, *Top. Catal.*, 2000, **10**, 107–113.

113 A. S. Eppler, G. Rupprechter, E. A. Anderson and G. A. Somorjai, *J. Phys. Chem. B*, 2000, **104**, 7286–7292.

114 S. Baldelli, A. S. Eppler, E. Anderson, Y. R. Shen and G. A. Somorjai, *J. Chem. Phys.*, 2000, **113**, 5432–5438.

115 J. P. R. Symonds, H. Arnolds, V. L. Zhang, K. Fukutani and D. A. King, *J. Chem. Phys.*, 2004, **120**, 7158–7164.

116 G. Rupprechter, M. Morkel, H.-J. Freund and R. Hirschl, *Surf. Sci.*, 2004, **554**, 43–59.

117 M. Morkel, G. Rupprechter and H.-J. Freund, *Surf. Sci.*, 2005, **588**, L209–L219.

118 M. Bäumer, J. Libuda, K. M. Neyman, N. Rösch, G. Rupprechter and H.-J. Freund, *Phys. Chem. Chem. Phys.*, 2007, **9**, 3541–3558.

119 D. Vogel, C. Spiel, Y. Suchorski, A. Trinchero, R. Schlögl, H. Grönbeck and G. Rupprechter, *Angew. Chem., Int. Ed.*, 2012, **51**, 10041–10044.

120 Y. Suchorski, I. Bespalov, J. Zeininger, M. Raab, M. Datler, P. Winkler and G. Rupprechter, *Catal. Lett.*, 2020, **150**, 605–612.

121 K. Wolter, O. Seiferth, H. Kuhlenbeck, M. Bäumer and H.-J. Freund, *Surf. Sci.*, 1998, **399**, 190–198.

122 A. F. Gusovius, T. C. Watling and R. Prins, *Appl. Catal., A*, 1999, **188**, 187–199.